The Kuiper Belt luminosity function from mR=22 to 25.

Jean-Marc C. Petit, M. J. Holman, Brett J Gladman, J. J. Kavelaars, H. Scholl, T. J. Loredo

Mon. Not. R. Astron. Soc. **365,** 429–438 (2006) doi:10.1111/j.1365-2966.2005.09661.x

The Kuiper Belt luminosity function from $m_R = 22$ to 25

J.-M. Petit,[1★†] M. J. Holman,[2,†] B. J. Gladman,[3,†‡] J. J. Kavelaars,[4,†] H. Scholl[3] and T. J. Loredo[5]

[1]*Observatoire de Besançon, BP 1615, 25010 Besançon cedex, France*
[2]*Harvard–Smithsonian Center for Astrophysics, MS-18, 60 Garden St., Cambridge, MA 02138, USA*
[3]*Observatoire de la Côte d'Azur, BP 4229, 06304 Nice cedex 04, France*
[4]*National Research Council Herzberg Institute of Astrophysics, 5071 West Saanich Road, Victoria, BC V9E 2E7, Canada*
[5]*Department of Astronomy, Cornell University, Ithaca, NY 14853, USA*

Accepted 2005 September 16. Received 2005 September 7; in original form 2005 February 25

ABSTRACT

In summer 1999, we performed a survey optimized for the discovery of irregular satellites of Uranus and Neptune. We imaged 11.85 deg^2 of sky and discovered 66 new outer Solar system objects (not counting the three new Uranian satellites). Given the very short orbital arcs of our observations, only the heliocentric distance can be reliably determined. We were able to model the radial distribution of trans-Neptunian objects (TNOs). Our data support the idea of a strong depletion in the surface density beyond 45 au.

After fully characterizing this survey's detection efficiency as a function of object magnitude and rate of motion, we find that the apparent luminosity function of the trans-Neptunian region in the range $m_R = 22$–25 is steep with a best-fitting cumulative power-law index of $\alpha \simeq 0.76$ with one object per deg^2 estimated at magnitude $R_{\rm o} = 23.3$. This steep slope, corresponding to a differential size index of $q \simeq 4.8$, agrees with other older and more recent analyses for the luminosity function brighter than 25 mag. A double power-law fit to the new data set turns out to be statistically unwarrented; this large and homogeneous data set provides no evidence for a break in the power-law slope, which must eventually occur if the Bernstein et al. sky density measurements are correct.

Key words: surveys – astrometry – Kuiper Belt – Solar system: formation.

1 INTRODUCTION

Over the past decade, a great deal of effort has been invested in the study of the small bodies of the outer Solar system, in particular the trans-Neptunian objects (TNOs), the Centaurs, and the irregular satellites of the giant planets. The trans-Neptunian region is especially attractive because its size distribution may hold clues to the process of giant planet formation (Davis & Farinella 1996; Gladman et al. 2001; Kenyon & Bromley 2004). The size distribution can be estimated from surveys which give their areal coverage and the TNO magnitudes (with errors), and which characterize their detection efficiency as a function of magnitude for each portion of their discovery fields. Published papers describing such surveys include Jewitt, Luu & Trujillo (1998), Gladman et al. (1998), Chiang & Brown (1999), Trujillo, Jewitt & Luu (2001a, hereafter TJL01), Larsen et al. (2001), Gladman et al. (2001), Trujillo et al. (2001b), Allen, Bernstein & Malhotra (2002), Trujillo & Brown (2003), and Bernstein et al. (2004). Bernstein et al. (2004) find a transition from a steep luminosity function at bright magnitudes to a shallower slope at faint magnitudes, implying that the index of the differential size distribution must change. Their best fit shows a luminosity function whose cumulative power-law slope begins to decrease at about an R-band magnitude of 23, for a double power-law functional form. However, the Bernstein et al. survey does not constrain the rollover magnitude very well due to the extreme faintness of the *Hubble Space Telescope* (*HST*) observations. We possess a data set very well suited to examining the behaviour of the luminosity function in the magnitude range $m_R = 22$–25.

We performed a survey in summer 1999 at the Canada–France–Hawaii Telescope (CFHT) aimed at discovering irregular satellites of Uranus and Neptune. This search was motivated by the discovery of the first two irregular moons of Uranus, Caliban (U XVI) and Sycorax (U XVII), in a cursory survey (Gladman et al. 1998). We imaged almost 6 deg^2 around both Uranus and Neptune to search for moving objects. Although the survey was optimized for detecting objects at 20- and 30-au heliocentric distances, it was also sensitive to the more distant TNOs out to distances of about 100 au.

★E-mail: petit@obs-besancon.fr
†Visiting Astronomer, Canada–France–Hawaii telescope, operated by the National Research Council of Canada, Centre National de la Recherche Scientifique de France, and the University of Hawaii.
‡Currently at Department of Physics and Astronomy, University of British Columbia, 6224 Agricultural Road, Vancouver, BC V6T 1Z1, Canada.

We discovered the Uranian irregular satellites Prospero, Stephano and Setebos (Gladman et al. 2000) in that run. Because our search method for irregular satellites is identical to that for TNOs (they are all moving objects after all), we also detected 66 additional moving objects. This paper describes these discoveries and their implications.

In Section 2 we give more details on the observational circumstances. In Section 3 we describe the data reduction procedures, and in Section 4 we present our analysis of the data set in terms of the luminosity function, inclination, and heliocentric distance distributions of the Kuiper Belt.

2 OBSERVATIONS

We were granted four nights of observations in 1999 July on the CFHT 3.6-m telescope on Mauna Kea. We used the CFH12K detector, a 12 288 × 8192 pixel mosaic of 12 2 × 4 K thinned, high-efficiency ($QE \sim 0.75$) CCDs (Cuillandre et al. 1999). At the CFHT $f/4$ prime focus, the camera has a pixel scale of 0.21 arcsec pixel^{-1}. Observations were made on the nights of July 18, 19, 20 and 21 UT. During this period, only 10 of the 12 CCDs were science quality, resulting in a usable field of view of $\sim$35 × 28 arcmin^2 $\simeq$ 0.27 deg^2. Images were taken through a Mould *R* filter, with a central wavelength of 6581 Å and a bandwidth of 1251 Å.

The weather conditions were very good for nearly the entire run. There was no time lost due to bad weather or wind. All data were obtained in seeing conditions between 0.7 and 1.2 arcsec. Fig. 1 presents seeing statistics over the four nights, demonstrating the uniformity of the image quality over the usable CCDs.

We chose a pattern of 24 fields (Fig. 2) around both Uranus and Neptune in order to cover the region of stable satellite orbits around these planets (Gladman et al. 2000). A 6 × 6 arcmin^2 region centred on the planet was avoided to reduce scattered-light problems. This field pattern was shifted nightly to follow each planet across the sky. Only 44 of these 48 pointings (listed in Table 1) were used in the analysis of this paper; we did not use the others as they showed photometric variations greater than 0.1 mag (for fields acquired at the very end of the July 19 UT night when minor cirrus arrived just before twilight). Each field was imaged three times for 480 s with about 40 min between exposures. We cycled through groups of four fields near one of the planets, in order to keep the airmass conditions roughly constant on a given field. At the time the observations were acquired, Neptune was about 5° from opposition and Uranus about 17°. At these elongations, outer Solar system objects are easily distinguished from foreground asteroids by their different rates of apparent motion in the sky.

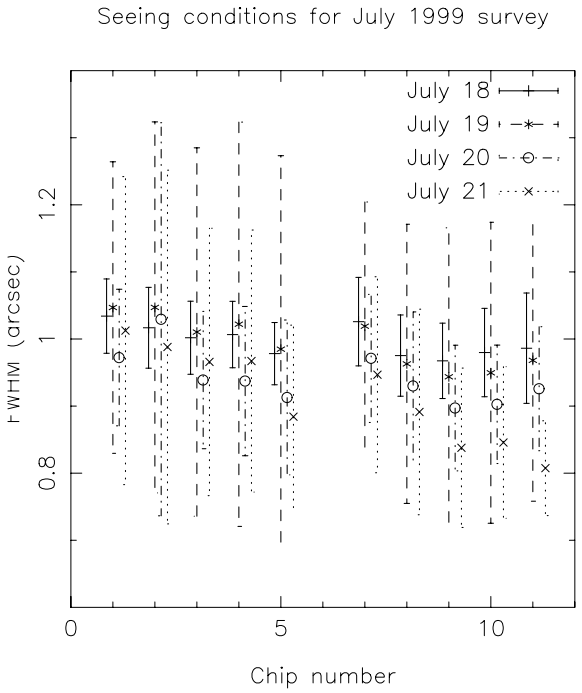

Figure 1. The mean FWHM, in pixels, with standard deviation, for each chip and each observing night during the 1999 July observing run. Chips 0 and 6, on the west side of the mosaic, were not of science grade during that run and were never processed.

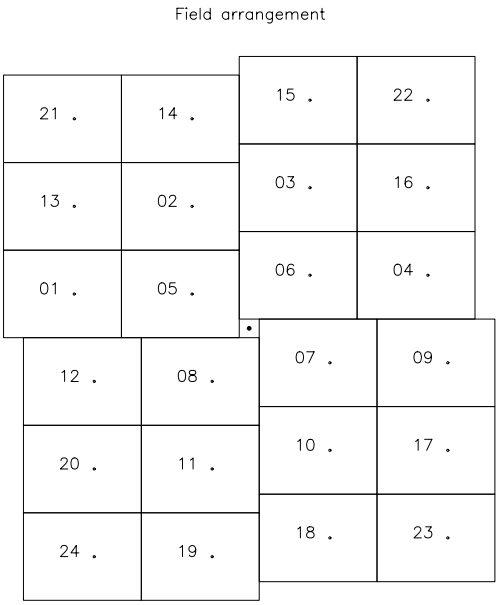

Figure 2. This figure shows the arrangement of CFH12K fields (each of 35 × 28 arcmin^2) relative to either Uranus or Neptune (the heavy dot). The open circle close to the centre of each field corresponds to the pointed right ascension and declination. The fields shown here correspond to the chips of science grade as of 1999 July. The two most western chips of the mosaic were never used in this survey.

3 DATA REDUCTION

3.1 Pre-processing

All chips of the mosaic were pre-processed simultaneously using the IRAF[1] MSCRED tools. The images were overscan corrected and bias subtracted (using an average of bias images obtained each night before twilight). The resulting images were flat-fielded to correct for instrumental sensitivity variations using the median of a series of short exposures acquired during evening twilight. The resulting images show sky backgrounds variations at or below 2 per cent.

The data presented in this paper were taken in photometric conditions. Photometric standards came from imaging Landolt standard field SA107 (Landolt 1992). For the five chips that had at least three

[1] IRAF is distributed by the National Optical Astronomy Observatories, which are operated by the Association of Universities for Research in Astronomy (AURA), Inc., under cooperative agreement with the National Science Foundation.

Table 1. List of pointings for our 1999 July CFHT observing run. The listed values correspond to the centre of the whole CFH12K mosaic. The two most western chips of the mosaic were never used in our survey, so the field of view for each pointing was about 35 × 28 arcmin^2, and extended from −14 to +14 arcmin in declination, and from +21 to −14 arcmin in right ascension from the listed values. Right ascension is given in hh:mm:ss.ss, declination in dd:mm:ss.ss and observing time in yyyy-mm-dd.ddddd. The UT date corresponds to the start of the first of three exposures on that field.

Field name	Right ascension	Declination	UT date
NEP1801	20:25:24.52	−18:59:02.27	1999-07-18.33446
NEP1802	20:22:54.19	−18:30:51.22	1999-07-18.34271
NEP1803	20:20:23.85	−18:24:51.22	1999-07-18.34978
NEP1804	20:17:53.52	−18:53:02.27	1999-07-18.35643
NEP1805	20:22:54.19	−18:59:02.27	1999-07-18.41916
NEP1806	20:20:23.85	−18:53:02.27	1999-07-18.42577
NEP1807	20:19:58.44	−19:21:13.32	1999-07-18.43245
NEP1808	20:22:28.77	−19:27:13.32	1999-07-18.43913
NEP1909	20:17:21.59	−19:21:35.73	1999-07-19.32508
NEP1910	20:19:51.94	−19:49:46.78	1999-07-19.33208
NEP1911	20:22:22.28	−19:55:46.78	1999-07-19.34030
NEP1912	20:24:52.62	−19:27:35.73	1999-07-19.34760
NEP1913	20:25:18.03	−18:31:13.62	1999-07-19.41629
NEP1914	20:22:47.69	−18:03:02.57	1999-07-19.42337
NEP2017	20:17:14.92	−19:50:09.78	1999-07-20.34533
NEP2018	20:19:45.27	−20:18:20.84	1999-07-20.35212
NEP2019	20:22:15.62	−20:24:20.84	1999-07-20.35906
NEP2020	20:24:45.98	−19:56:09.78	1999-07-20.36591
NEP2121	20:25:04.73	−18:03:48.57	1999-07-21.34283
NEP2122	20:17:33.66	−17:57:48.57	1999-07-21.35001
NEP2123	20:17:08.25	−20:18:43.84	1999-07-21.35666
NEP2124	20:24:39.32	−20:24:43.84	1999-07-21.36341
URA1805	21:14:20.88	−16:38:51.57	1999-07-18.50972
URA1806	21:11:52.52	−16:32:51.57	1999-07-18.51659
URA1807	21:11:27.45	−17:01:02.63	1999-07-18.52329
URA1808	21:13:55.80	−17:07:02.63	1999-07-18.53013
URA1902	21:14:12.08	−16:11:20.82	1999-07-19.51287
URA1903	21:11:43.71	−16:05:20.82	1999-07-19.51971
URA1904	21:09:15.34	−16:33:31.87	1999-07-19.52642
URA2009	21:08:41.38	−17:02:23.53	1999-07-20.43475
URA2010	21:11:09.76	−17:30:34.58	1999-07-20.44307
URA2011	21:13:38.13	−17:36:34.58	1999-07-20.45972
URA2012	21:16:06.51	−17:08:23.53	1999-07-20.46769
URA2013	21:16:31.59	−16:12:01.42	1999-07-20.52968
URA2014	21:14:03.21	−15:43:50.36	1999-07-20.53648
URA2015	21:11:34.84	−15:37:50.36	1999-07-20.54383
URA2016	21:09:06.46	−16:06:01.42	1999-07-20.55053
URA2117	21:08:32.23	−17:31:16.28	1999-07-21.42694
URA2118	21:11:00.62	−17:59:27.34	1999-07-21.43376
URA2119	21:13:29.01	−18:05:27.34	1999-07-21.45496
URA2120	21:15:57.39	−17:37:16.28	1999-07-21.53100
URA2121	21:16:22.47	−15:44:32.06	1999-07-21.53766
URA2122	21:08:57.31	−15:38:32.06	1999-07-21.54439
URA2123	21:08:32.23	−17:59:27.34	1999-07-21.55107

standard stars, the zero-points were estimated individually; these were identical to within 0.02 mag. This uniformity was introduced by the data mosaic reduction process, which reset the effective gains on the CCDs so they all had the same zero-point. This allowed us to carry out photometry on all CCDs, even if we did not have enough standards to independently measure the zero-point.

Because the standard images were acquired at an airmass of $\simeq$1.06, we did not directly measure the airmass term in the photometric transformation. We take it to be 0.08 per airmass, as measured on our previous CFHT data (Gladman et al. 2001). Because of the limited number of standard stars on each CCD, we combined them all (because the zero-points are compatible between chips) to slightly improve the determination of the colour term. The average colour of the standards used is $V{-}R = 0.5$, typical of TNOs (Doressoundiram et al. 2005). Although we do not have great confidence in the colour term, it has little effect on the photometric zero-point over reasonable colour variations. Our final photometric transformation is

$$R = -2.5 \log \frac{F}{1\ \mathrm{ADU\,s^{-1}}} - [0.03(V{-}R)] - (0.08\ \mathrm{airmass}) + 26.12 \pm 0.03, \quad (1)$$

where F is the flux received from the object.

The airmass of our science images varied from 1.25 to 1.99, with an average value of 1.43. Using the typical TNO $V{-}R = 0.5$, the average airmass plus colour correction in the previous formula is -0.13 ± 0.04 mag for an average zero-point of 25.99 ± 0.05. We thus used a final (1 ADU s^{-1}) zero-point of 26.0 for all our work, accurate to several hundredths of a magnitude. Most of our detected TNOs have typical photometric errors of about one- or two-tenths of a magnitude, dwarfing the zero-point uncertainties.

3.2 Artificial object addition

For each triplet of images and for each CCD independently, we registered the images, i.e. we shifted the second and third images so that each star would have the same pixel coordinates as in the first image. Once all images had been registered, we used the IRAF FIND and DAOPHOT tools on each individual frame to determine the point spread function (PSF) of that frame. We found that the PSF did not vary significantly within the individual CCDs. Using this PSF, we then incorporated artificial objects into the data. For each triplet we inserted a random number of artificial objects (35–50, with an average number of 42 per CCD), with randomly chosen R magnitudes in the range 20–26, rates of motion from 1 to 10.5 arcsec h^{-1}, and angle from 2° to 46° south of due west, corresponding to ecliptic position angles from −32.8° to 11.2°. At opposition, these rates of motion would be exhibited by outer Solar system objects on circular orbits at distances from 10 and 150 au. The range of directions encompass almost all possible directions of TNO motion at opposition due to orbital inclination (up to 60° inclination). In implanting the objects, we accounted for their motion during the 480-s exposures by dividing the exposure time by 10 and implanted 10 'subobjects' with one-tenth of the flux, at centroids moving according to the rate and direction of motion of the desired object. Our artificial objects thus correctly mimic trailing losses when moving at rates comparable to or larger than the FWHM during a single exposure (see below).

Note that the actual seeing of each individual image is correctly accounted for in our efficiency function calculations (below) because each image has its own PSF constructed from stars present on that image; in particular, our implanted objects vary their FWHM if the seeing varies between frames (allowing artificial objects to fade below the detection limit if the seeing degrades, for example).

3.3 Moving object detection

Once the images have been planted with artificial objects, we ran our semi-automated detection code, as described by Petit et al. (2004), except that we used only the wavelet method to detect the moving objects. We set the detection limits to rates of motion between 0.8 and 11 arcsec h^{-1} and directions between 1° and 49° in angle to the

south of due west (that is, at realistic angles relative to the ecliptic plane on the sky). The code detected real objects, artificial objects and false candidates (mostly generated along the diffraction spikes of bright stars and in the wings of extended background galaxies). Human operators visually checked each and every automatically detected object to accept it as real (i.e. a real TNO or a implanted object) or to reject it as a spurious detection of noise fluctuations. This verification process was very long and tedious, occupying five of us full time for about one week; however, as explained below we believe this visual inspection of all detected objects is critical to correctly determine the detection efficiency.

3.4 Efficiency functions

After operator inspection of all candidates, we compared the list of operator-verified objects with the list of artificial implanted objects. We thus obtained a list of real outer Solar system objects and the list of fake objects that we were able to detect. From this latter list, we can measure our detection efficiency as a function of both magnitude and rate of motion.

Fig. 3 shows the efficiency of detection as a function of the magnitude of the objects. During the four nights of our run, the seeing conditions were somewhat poorer (1.1-arcsec seeing) at the start of the night and then stabilized to subarcsecond conditions. Because Neptune was at lower right ascension and visible first, the image quality is on average poorer for the fields near Neptune than for those near Uranus. Thus, our survey is sensitive to fainter objects near Uranus. This is reflected in the efficiency curves, which have been computed separately for the fields around each of the two planets; the data through which the efficiency curve is fit are shown only for Uranus. The efficiency $\eta(R)$ is well modelled by a function with two hyperbolic tangents:

$$\eta(R) = \frac{A}{4}\left[1 - \tanh\left(\frac{R - R_c}{\Delta_1}\right)\right]\left[1 - \tanh\left(\frac{R - R_c}{\Delta_2}\right)\right]. \quad (2)$$

Here, the fitted parameters A, R_c, Δ_1 and Δ_2 denote the amplitude (maximum efficiency), roll-over magnitude and widths of the two components, respectively. We found that the faint-magnitude end of these efficiency curves could not be well represented by the single hyperbolic tangent model that we have used previously in our pencil-beam work; the greater variety of seeing conditions in this work produces a softer initial drop at brighter magnitudes and a longer tail at the faint end (due to a few exceptional-seeing triplets allowing the detection of a few very faint TNOs).

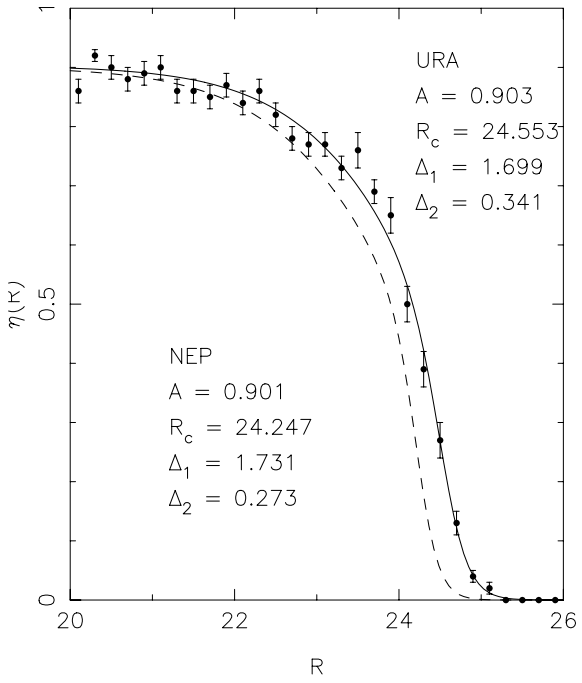

Figure 3. The TNO detection efficiency as a function of R-band magnitude for the two halves of the survey. The dashed curve gives the best fit to the TNO efficiency near Neptune. The solid curve and points give efficiency data and the best fit for the fields taken near Uranus. The quality of the fit to the efficiency data points near Neptune (not shown) is comparable to that near Uranus. The best-fitting parameters to the functional form of equation (2) are given. The fields near Uranus are roughly 0.3 mag deeper due to the consistently better seeing in the second halves of our nights.

At magnitudes brighter than about 22 mag, only 90 per cent of the surface area is effectively used for discovering objects, due to background confusion from stars and galaxies, CCD cosmetic flaws, and the finite size of the chips. The finite size of the CCDs implies that an object close to the western edge on the first exposure will move off the CCD (retrograde motion) on the subsequent images and fall in a gap between CCDs in the mosaic. As explained in Gladman et al. (2000), about 3 per cent of the field area is occupied by bright stationary objects and CCD flaws, resulting in a loss of ∼9 per cent of the field for detection because objects move several FWHMs between frames, and so the problem repeats for every exposure. The non-detection of ≃10 per cent of the bright artificial objects is sensible.

The completeness magnitude R_c, defined as the magnitude where our detection efficiency falls to 50 per cent of its maximum value (here this corresponds to an efficiency of about 45 per cent), is $R_c = 24.25$ for the fields near Neptune and $R_c = 24.55$ near Uranus. Both subsurveys show similar shape parameters for the widths Δ_i and maximum efficiencies A (shown in Fig. 3).

Another interesting indicator is the efficiency of detection as a function of rate of motion (Fig. 4). For bright objects ($m_R < 22$), the detection rate is nearly constant around 85–90 per cent with a mild decrease to 80–85 per cent efficiency for rates $\geqslant$8 arcsec h^{-1}. For fainter objects in our survey ($23 < m_R < 25$), this effect is more pronounced because trailing loss can reduce their signal-to-noise to below the detection limit. These fast rates correspond to motions that become comparable to the seeing in a single exposure; however, because they correspond to heliocentric distances inside Uranus this effect is irrelevant for our examination of the trans-Neptuian region. Fig. 4 also exhibits a decrease in efficiency for rates slower than 2 arcsec h^{-1}. Our algorithm rejects objects that display significantly non-linear motion, as well as objects moving at rates below a specified threshold. Thus, when the number of pixels moved between the first and third exposures is small, small errors of centroiding and registration result in more objects being rejected as spurious. Thus, our survey is somewhat less sensitive to TNOs further than 75 au, corresponding to a rate of motion of ∼2 arcsec h^{-1} at opposition, although the drop in sensitivity is small out to 100 au.

4 ANALYSIS

A first detection pass was performed in near real time at the telescope to search for satellites of Uranus and Neptune, the primary goal of our observing run. This initial search was performed on images that were not yet augmented with artificial objects, and therefore is not characterized. Artificial object implantation and the full re-examination of the photometric fields were performed after the

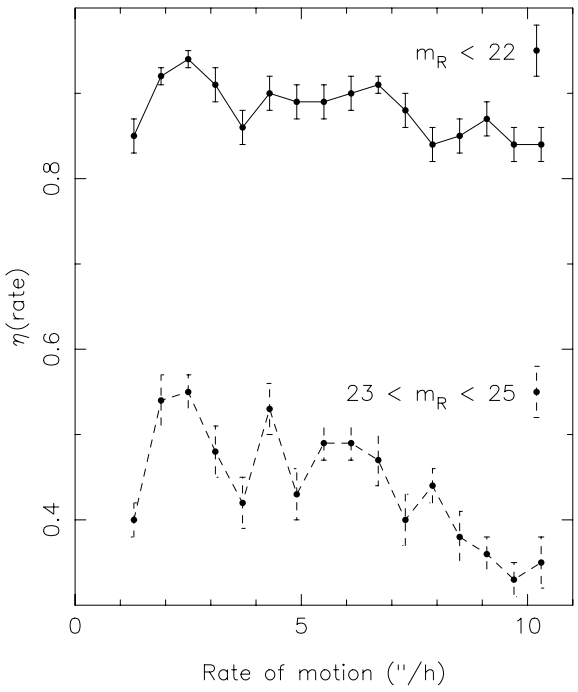

Figure 4. The dependence of our detection efficiency upon rate of motion on the sky. The solid line shows objects brighter than magnitude $m_R = 22$, and the dashed line objects with magnitude m_R in the range 23–25. These results are integrated over all fields and all CCDs. See text for discussion.

observing run. Because we used a slightly different approach for the characterized detection, using different parameters in the detection code trying to reach slightly fainter magnitudes than was possible in near real time at the telescope due to the false-detection rate, we found a slightly different set of objects. In particular, one TNO found by us at the telescope was not found in the characterized detection and we thus ignore this object in the present analysis. Additionally, several TNOs were discovered in fields of non-photometric quality at the telescope and these fields and the objects contained in them are also excluded from the present characterized analysis.

66 moving objects were discovered in the characterized survey (Table 2). One of these, here designated as NL224, which we subsequently tracked and which was designated 1999 OX3 by the Minor Planet Centre, was originally taken as a candidate Neptunian irregular satellite due to its proximity to Neptune both in angular separation and heliocentric distance; tracking by us weeks later showed this object to be a large ($D \simeq 200$ km) Centaur and not a TNO. We thus removed this object for the remaining analysis, leaving 65 TNOs in our sample.

Because our principal objective was to discover Uranian and Neptunian satellites, we did not acquire a second night of observation for all the fields, but only for those where a candidate moon (with larger retrograde motions than the TNOs due to their proximity) had been identified. As a result, many of the objects reported here were seen on only a single night. However, in all cases where we obtained images on a second night from the CFHT (due to re-imaging while following up a satellite candidate), the objects detected on the first night appeared on the second night. In addition, we have performed additional tracking observations (described elsewhere) for some of this sample's TNOs; all such objects searched for were recovered. Each time an object was in one of our recovery fields and above our magnitude limit, it was recovered. We are confident that all objects reported in Table 2 are indeed real TNOs.

Table 2. Objects discovered within the characterized survey, ordered by *R*-band apparent magnitude. Diameters are computed assuming albedos of 0.04, and may be wrong to a factor of 2. The heliocentric distances *r*, orbital inclinations and associated errors were computed using the ORBFIT package of Bernstein & Khushalani (2000), version 2.0. A star in column 'Recov.' means the object was recovered on later night(s).

Name	Recov.	m_R	r (au)	D (km)	Inclination
NL224	*	21.53 ± 0.06	28 ± 3	214	5 ± 17
NI073	*	22.07 ± 0.06	39 ± 6	334	16 ± 34
UL218	*	22.70 ± 0.07	45 ± 7	328	7 ± 36
UK132	*	22.80 ± 0.08	41 ± 6	255	2 ± 31
UK105b	*	23.00 ± 0.07	40 ± 6	226	18 ± 30
NJ134a	*	23.15 ± 0.07	45 ± 8	262	25 ± 47
UI08A	*	23.15 ± 0.07	45 ± 8	263	2 ± 31
NK17B	*	23.25 ± 0.07	42 ± 6	223	2 ± 33
UI08Bb	*	23.30 ± 0.36	40 ± 2	199	2 ± 0
UK097a	*	23.30 ± 0.08	35 ± 4	154	6 ± 21
NI075		23.33 ± 0.17	39 ± 6	186	20 ± 36
UL215a	*	23.33 ± 0.09	43 ± 7	226	2 ± 33
NI071		23.40 ± 0.14	45 ± 7	239	8 ± 39
NK188		23.43 ± 0.12	41 ± 6	199	7 ± 33
UJ03A	*	23.53 ± 0.24	41 ± 5	186	0 ± 20
UK122	*	23.53 ± 0.06	43 ± 8	201	22 ± 42
NI061	*	23.60 ± 0.07	42 ± 6	187	5 ± 33
UK157		23.60 ± 0.08	40 ± 7	169	17 ± 35
NI053	*	23.63 ± 0.12	37 ± 6	145	21 ± 34
NK179	*	23.65 ± 0.15	39 ± 6	162	9 ± 31
NJ13Ba		23.70 ± 0.08	38 ± 5	146	1 ± 27
UK105a		23.70 ± 0.08	41 ± 6	172	15 ± 29
UK15B		23.73 ± 0.09	38 ± 6	146	12 ± 31
NJ113	*	23.77 ± 0.24	43 ± 7	185	15 ± 37
NK192		23.77 ± 0.21	39 ± 6	147	23 ± 38
NI037	*	23.85 ± 0.14	43 ± 6	175	2 ± 30
NL218	*	23.87 ± 0.17	39 ± 6	147	5 ± 29
UL181a		23.87 ± 0.12	44 ± 6	183	10 ± 29
NJ14B	*	23.90 ± 0.14	43 ± 6	169	1 ± 17
NL21A	*	23.90 ± 0.20	44 ± 8	176	25 ± 46
UK097b	*	23.90 ± 0.20	45 ± 6	187	13 ± 32
NJ097		23.93 ± 0.12	39 ± 9	142	38 ± 58
NJ109	*	23.97 ± 0.17	42 ± 7	160	19 ± 37
NJ124		24.00 ± 0.33	43 ± 7	165	9 ± 35
NJ13Bb		24.00 ± 0.14	37 ± 5	119	9 ± 27
NI049		24.03 ± 0.12	41 ± 6	149	8 ± 32
NK209		24.03 ± 0.12	36 ± 6	112	27 ± 38
NJ129	*	24.07 ± 0.19	39 ± 6	132	14 ± 32
UI08Ba	*	24.07 ± 0.29	40 ± 2	139	1 ± 0
UK155		24.07 ± 0.12	43 ± 9	159	29 ± 50
UL233		24.07 ± 0.12	45 ± 7	171	1 ± 14
UK148		24.10 ± 0.16	40 ± 6	134	2 ± 30
NI022		24.13 ± 0.21	35 ± 5	103	4 ± 24
NJ134b	*	24.13 ± 0.21	43 ± 6	153	7 ± 34
UK101		24.13 ± 0.12	41 ± 5	140	4 ± 26
UL221		24.13 ± 0.12	40 ± 6	135	11 ± 31
UL195		24.17 ± 0.12	39 ± 6	124	2 ± 19
NI051	*	24.20 ± 0.12	46 ± 9	174	20 ± 46
UK134	*	24.27 ± 0.12	46 ± 8	165	1 ± 37
UK169		24.27 ± 0.12	40 ± 7	125	17 ± 35
UK118		24.30 ± 0.12	38 ± 6	111	5 ± 26
UL17A		24.30 ± 0.14	45 ± 6	154	19 ± 33
UL192a		24.30 ± 0.22	44 ± 8	148	17 ± 40
UL227		24.30 ± 0.14	40 ± 6	124	16 ± 32
UL215b	*	24.45 ± 0.15	43 ± 7	132	12 ± 34
UL184		24.50 ± 0.12	45 ± 6	140	3 ± 26
UK113		24.53 ± 0.12	32 ± 4	73	3 ± 19
UL229		24.57 ± 0.12	44 ± 7	130	9 ± 34
UK165		24.60 ± 0.12	48 ± 9	153	5 ± 40

Table 2 – *continued*

Name	Recov.	m_R	r (au)	D (km)	Inclination
UL181b		24.60 ± 0.14	48 ± 9	156	32 ± 50
UL204		24.60 ± 0.14	39 ± 6	101	6 ± 27
UL207		24.67 ± 0.24	50 ± 9	162	3 ± 33
UL209		24.67 ± 0.12	41 ± 6	111	2 ± 22
UL208		24.73 ± 0.21	37 ± 5	89	3 ± 22
UL238		24.73 ± 0.21	39 ± 6	94	11 ± 29
UL192b		24.97 ± 0.17	45 ± 8	115	15 ± 41

The nomenclature for these TNOs is as follows. The first letter indicates the planet near which the object was discovered. The next letter indicates the UT date in 1999 July of the discovery triplet with the code I = 18, J = 19, K = 20 and L = 21. The next two digits indicate the field number from our rosette near the planet (Fig. 2). The next character indicates the mosaic CCD number in which the object was discovered (with A = CCD 10 and B = CCD 11). Lastly, an 'a' or 'b' may be added if two TNOs were discovered in the same CCD. So, UK113 is the TNO discovered on CCD 3 of field 11 near Uranus on 1999 July 20 UT.

4.1 Trans-Neptunian Objects

26 of the 65 TNOs were discovered in fields near Neptune, and 39 near Uranus. Our effective area (that is, the amount of sky actually searched in our characterized survey) is 5.88 deg^2 near Neptune and 5.97 deg^2 near Uranus. Many of the TNOs near Uranus were discovered in the run's very best seeing conditions, explaining the greater numbers near that planet. We measure the apparent magnitude of the TNOs on the three discovery images and give the mean magnitude and rms photometric error derived from DAOPHOT (neglecting a possible tiny systematic offset in the system's photometric zero-point as discussed above). Our brightest TNO (neglecting the Centaur NL224) is NI073 just fainter than 22 mag. Using our previous best-fitting luminosity function (Gladman et al. 2001), the cumulative surface Σ density expected at 22 mag is $\log_{10} \Sigma(<22) = 0.69\,(22\text{–}23.5) = -1.04$ or $\Sigma(<22) = 0.093$ objects per deg^2. One would have to search 11 deg^2 to expect to find an object this bright, whereas we searched 12 deg^2 with roughly 90 per cent efficiency to find NI073. A more rigorous approach is to compute the probability distribution of the magnitude of the brightest object in a data set of 65 samples for this luminosity function. The most likely magnitude for the brightest object is then 21.65, while the expectation value is 21.3. Using the luminosity function determined in the current work (see Section 4.3), we find a most likely magnitude of 21.9 and an expectation value of 21.6. The magnitude of NI073 is consistent with both luminosity functions, although slightly closer to what the current work predicts.

Using the apparent R-band magnitudes, we have estimated diameters neglecting phase effects and using a 4 per cent geometric albedo (for ease of comparison with earlier work). The resulting diameters (listed in Table 2) are no more accurate than about 50 per cent given the photometric uncertainties and uncertainties in the geometric albedo.

The 65 TNOs exhibit heliocentric distances at discovery ranging from 32 to 50 au; these instantaneous distances are usually about 10–20 per cent accurate due to the very short observational arc (two TNOs were seen on two nights and thus have 5 per cent distance uncertainties). These distances have been estimated by the Minor Planet Centre and by the orbit-fitting algorithm of Bernstein & Khushalani (2000). Orbital inclinations are also given; the uncertainties in these are very large due to the 2-h arcs.

4.2 Inclination and radial distributions

Thanks to early discovery and/or subsequent surveys of the same part of the sky, a subset of 29 objects from our sample has been followed over multiple oppositions, allowing a precise determination of their orbital elements and distance at discovery.

Brown (2001) proposed a robust method to determine the inclination distribution even from short arc orbits, assuming that the inclination is correctly determined from the first observations. However, for our very short arcs, the inclination uncertainties are so large that we are doubtful that Brown's method can be applied. We have compared this short arc inclination distribution to the inclination distribution of the multi-opposition subset. We applied Kuiper's modified Kolmogorov–Smirnov test (Press et al. 1992) to see if both samples were drawn from the same distribution. We found that the hypothesis that both samples are drawn from the same distribution can be rejected at the 99.8 per cent confidence level. So it is not relevant to apply Brown's method to the inclination distribution of our sample, and we have decided not to make any conclusions regarding the inclination distribution.

Several authors have presented evidence for an edge of the classical Kuiper belt (Dones 1997; Jewitt et al. 1998; Trujillo & Brown 2001; Trujillo et al. 2001a; Allen et al. 2002). To see if our data support such a claim, we apply the simple debiasing method of Trujillo & Brown (2001). This consists simply of multiplying the apparent radial distribution $f_{\rm app}(d)$ by a normalized bias-correction factor $\beta(d) = [(d^2 - d)/(d_0^2 - d_0)]^{q-1}$ where d is the heliocentric distance, q is the size distribution power-law index, and d_0 is an arbitrary normalization factor; we used $d_0 = 43$ au. q is simply related to the luminosity function slope α by $q = 5\alpha + 1$ (Gladman et al. 2001). This yields the intrinsic heliocentric distance distribution $f(d)$, to within a factor $\Gamma\prime(m_v)^{-1}$ depending only on the observed magnitude of the objects (see Trujillo & Brown 2001 for a precise definition of all terms). The data points with the solid error bars (representing the Poissonian 68 per cent confidence limit on the apparent number of objects; Kraft, Burrows & Nousek 1991) in Fig. 5(a) show the intrinsic heliocentric distance distribution $f(d)$ computed from the observed distance distribution, assuming a size distribution power-law index $q = 4.8$ (our best-fitting value, with $q = 5\alpha + 1$). Clearly, we see a strong depletion beyond 46 au, although there are quite a few objects at distances around 50 au. The derivation of the bias-correction factor relies on three assumptions: (i) all Kuiper Belt objects follow the same size distribution described by a differential power law; (ii) the albedo is not a function of radius r nor heliocentric distance d; (iii) observations are conducted at opposition allowing the transformation geocentric distance $\Delta = d - 1$ au. Satisfying assumptions (i) and (ii) is beyond our control. However, assumption (iii) directly depends on the survey and is very well satisfied in our case, $\Delta = d - 1$ au never being violated by more than 0.05 au.

We computed the probability of finding our farthest object at a heliocentric distance of 50 au, for a sample of 65 objects. To do so, we constructed a disc model with an inner edge at 35 au (the heliocentric distance of our innermost object), with luminosity function of slope $\alpha = 0.76$ and a volume number density in the ecliptic declining radially as a power law with index β (see Gladman et al. 2001). For $\beta = 2$, the probability that our outermost object is at 50 au is only 0.0014 and for $\beta = 3$, it is only 0.008.

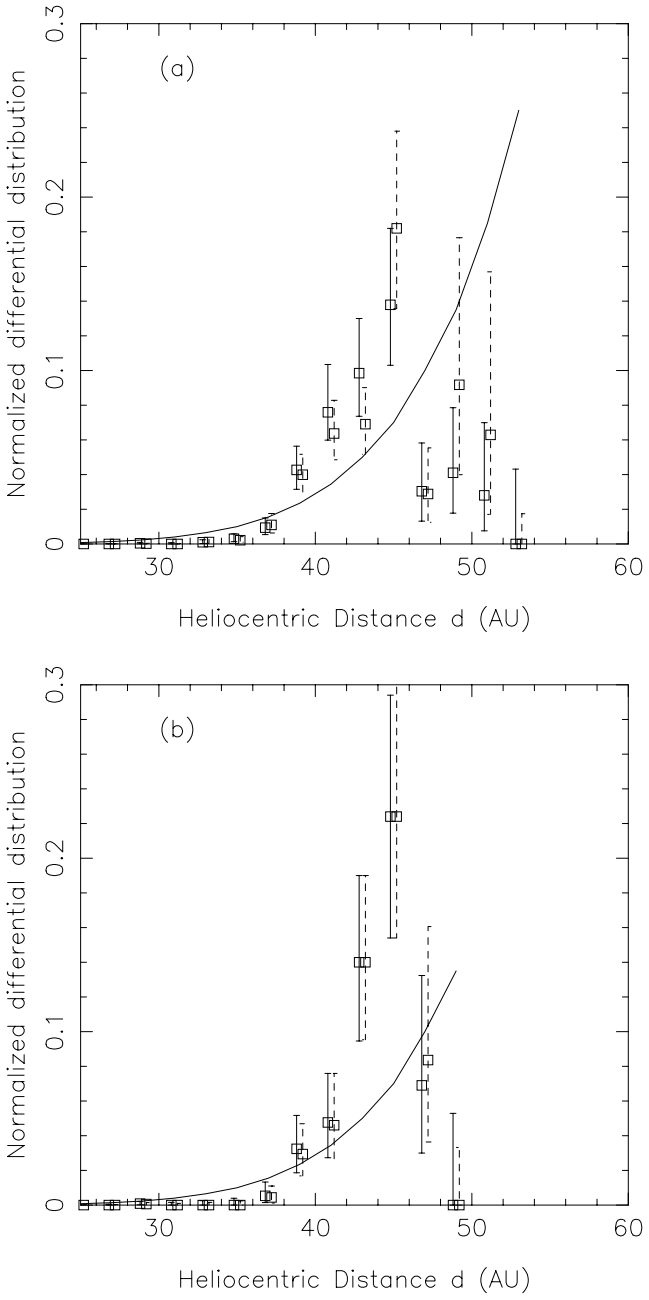

Figure 5. Binned intrinsic heliocentric distance distribution for a $q = 4.8$ differential size distribution, with Poissonian error bars. Data points with solid error bars correspond to the observed distribution multiplied by the bias-correction factor $[(d^2 - d)/(d_0^2 - d_0)]^{q-1}$ as defined by Trujillo & Brown (2001), where d_0 is an arbitrary normalization constant. Data points with dashed error bars include correction by the magnitude efficiency factor. Both distributions have been normalized to 1. The solid line represents the correction factor from apparent to intrinsic distributions (divided by 20 to fit into the plot). (a) Full data set of 65 objects. (b) Subset of multi-opposition objects.

According to Trujillo & Brown (2001), the magnitude-dependent bias (discovery efficiency) is independent of heliocentric distance, and hence acts as a constant factor when transforming from the apparent distribution to the intrinsic distribution. To test this hypothesis, points with dashed error bars in Fig. 5(a) show the intrinsic radial distribution obtained by correcting the apparent distribution for detection efficiency. In the apparent distribution, each object is no longer counted as a single event but rather as a $1/\epsilon(m_v)$ event, where $\epsilon(m_v)$ is the efficiency of detection at magnitude m_v. Although this does not change the conclusion on the strong depletion beyond 47 au, the intrinsic distribution is noticeably changed when we account for detection efficiency, although the difference is of the order of 1σ.

As mentioned before, there is a loss of efficiency of detection of faint objects at rates slower than 2 arcsec h^{-1}. For observations at opposition, this corresponds to objects at about 65 au and beyond. Thus, this loss of efficiency cannot explain the depletion beyond 47 au.

In order to check if the heliocentric distance distribution determined from the discovery observations alone is representative, we compared it to the same distribution for the multi-opposition subset. We applied Kuiper's modified Kolmogorov–Smirnov test (Press et al. 1992) to see if both samples were drawn from the same distribution. This hypothesis can be rejected only at the 39.9 per cent confidence level, i.e. we cannot disprove the hypothesis. We thus applied the bias-correction algorithm from Trujillo & Brown (2001), and found a strong depletion beyond 45–47 au, as expected (Fig. 5b).

If we assume now a double power law for the luminosity function, the bright end has a much steeper slope of $\alpha_1 = 1$ for our best fit, or $\alpha_1 = 1.08$ for the Bernstein et al. (2004) best fit. This larger value of the slope increases the correction factor, but not enough to compensate for the depletion beyond 47 au. For these values of the slope, the probability of finding our farthest object at 50 au is only 3.5–7.5 per cent, while the most likely location of the farthest object varies from 51 to 55 au. Thus, if the luminosity function is really as steep as the most extreme modern estimates, the statistical significance of the surface density drop-off at around 47 au is at the 2σ level.

Levison & Morbidelli (2003) proposed a model for the formation of the outer Solar system with a disc of planetesimals initially truncated around 30–35 au. This disc is later pushed outward by Neptune's 1:2 mean motion resonance during its final phase of migration. This predicts an edge of the belt at the current location of Neptune's 1:2 mean motion resonance at 48 au. The depletion seen in our data seems to begin slightly closer to the Sun, but may still be consistent with this model, especially because the proposed theoretical edge occurs in the semimajor axis distribution, and we are looking at the distance distribution. Weidenschilling (2003) proposed another model where an outer edge of the planetesimal swarms naturally occurs somewhere between 40 and 50 au due to gas drag. The exact location of the edge is mostly sensitive to the gradient of surface density of the nebula.

4.3 Luminosity function

The trans-Neptunian luminosity function serves as a surrogate for the size distribution due to fact that the albedos are unknown. For a single power-law formulation, the cumulative surface density Σ of TNOs (per deg^2) with magnitude brighter than m_R is

$$\log_{10} \Sigma(<m_R) = \alpha(m_R - R_o), \tag{3}$$

where R_o is the magnitude at which Σ equals 1 TNO per deg^2 and α is the slope of the cumulative luminosity function of $\log_{10} \Sigma$ versus m_R. In this formulation a power law of slope α would imply a differential diameter distribution with power-law index $q = 5\alpha + 1$. Recent estimates of single power-law slopes for the Kuiper Belt vary in the range $\alpha = 0.6$–0.9, but Bernstein et al. (2004) suggest double and rolling power-law fits to produce shallower slopes

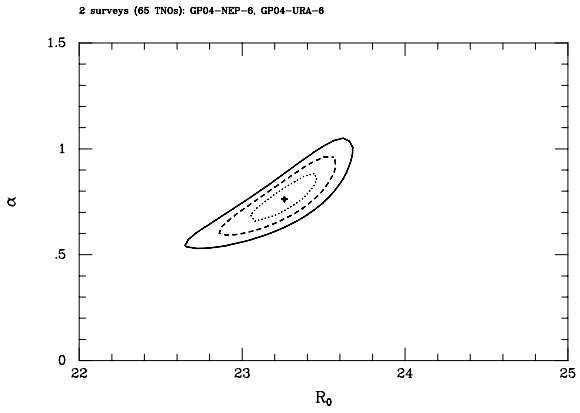

Figure 6. Credible regions for the single power-law fit to the 65 TNOs used in the present work. Contours show boundaries of 68.3, 95.4 and 99.7 per cent credible regions, i.e. contours of constant joint probability for α and $R_{\rm o}$ enclosing the given fraction of the total probability. The point show the best-fitting parameters $(\alpha,\, R_{\rm o}) = (0.76, 23.3)$.

at faint magnitudes to explain the lack of TNO detections seen in their very deep *HST* imaging experiment. Our present work offers the advantages of having a large sample of detected objects (65) found in a highly homogeneous survey over four nights, all at similar ecliptic latitude and longitude, and which has been exhaustively characterized by human operators. The most similar survey is that of TJL01 in which they detected 74 TNOs within 2° of the ecliptic but with a wide range of ecliptic longitude. Because the sky density of TNOs is expected to vary with ecliptic longitude (due to mean motion resonances which confine perihelia of TNOs to certain longitudes relative to Neptune) and latitude, our present work is more uniform (Uranus and Neptune being only 15° apart in the sky).

Applying the Bayesian analysis discussed in Gladman et al. (1998, 2001), we proceeded to fit a single power-law model, to this homogeneous data set alone. The joint credible regions for the analysis are shown in Fig. 6, giving best-fitting parameters of $\alpha = 0.76$ and $R_{\rm o} = 23.3$ (with the joint uncertainty being shown in the figure). These values are essentially the same as those obtained in Gladman et al. (1998). Because we noted above a difference in limiting magnitude for the Neptune and Uranus fields, we also fitted the two subsets separately. For the Uranus subset, we find $\alpha = 0.76$ and $R_{\rm o} = 23.3$, and for Neptune $\alpha = 0.84$ and $R_{\rm o} = 23.3$. Both fall well within the credible region of the full set fit and their individual credible regions essentially overlap each other and that of the full set, only extending further out. So the two luminosity distributions are perfectly consistent. For comparison, the best-fitting parameters found by TJL01, $(\alpha,\, R_{\rm o}) = (0.63, 23.04)$ (see below for more details), fall mid-way between the 68.3 and 95.4 per cent curves. Because of the large number of detections, we have plotted the sky density estimates in Fig. 7 in terms of differential numbers of TNOs per deg^2 per magnitude. The sky density estimates have been bias-corrected and the displayed error bars incorporate Poisson errors due to small numbers and the estimated uncertainty in the detection efficiency. The solid data points show the differential sky density estimates when 0.5-mag bins are begun at $m_R = 22.0$ and the efficiencies used are at the bin centre. This representation corresponds very well to the best-fitting cumulative single power law (solid line) when translated to the differential formulation. The data points with dotted error bars represent the surface density estimates with a binning that differs only by beginning at a different magnitude; a least-squares fit to these data points would give a different result. This demonstrates the inherent danger of fitting luminosity functions to binned differential estimates.

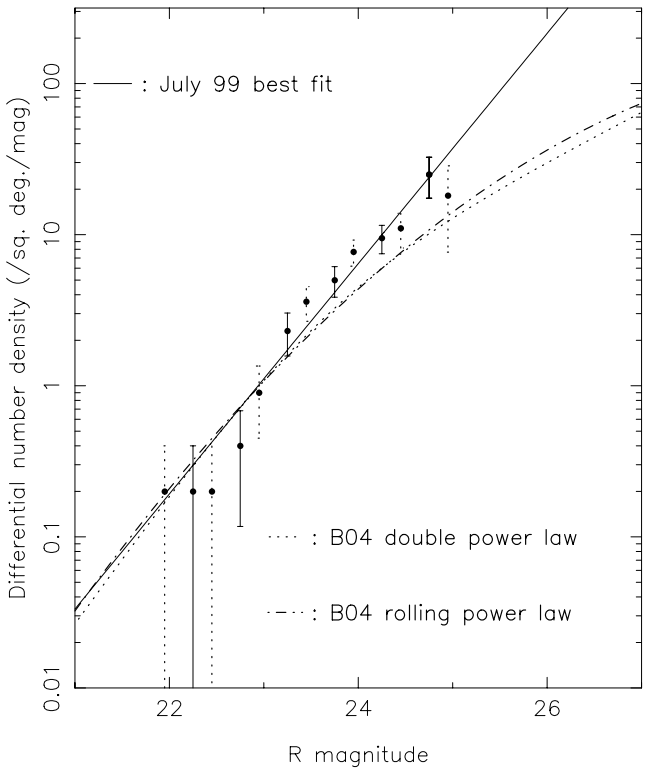

Figure 7. The TNO differential surface density (per magnitude per deg^2) as a function of R magnitude, derived only from the 1999 detections near Uranus and Neptune. The solid line shows our derived best-fitting single power law from these data alone, fit via a maximum likelihood method. The solid data points show one possible representation of the data set, binned in 0.4-mag width bins; this set of bin borders shows a satisfactory match to the single power law. The dashed points show exactly the same data, but with different bin centres. The single power law provides a slightly better fit to the data set, but see text for further discussion. The proposed double power-law and rolling power-law fits of Bernstein et al. (2004) to literature surveys are shown for comparison as the dashed lines; for magnitudes above $R = 23$, this behaviour is indistinguishable from the single power law. Fainter than 23 mag these two fits predict fewer TNOs than we observe.

To the eye, this dotted representation seems to show some evidence for a shallower slope at the faint end, more along the lines of the rolling or double power-law fits which come from the Bernstein et al. (2004) analysis of published surveys (but which is essentially entirely controlled by the *HST* survey). We have explored the evidence for a departure from a single power law in our data set alone in two ways. First, we fit a double power-law differential surface density to our data set in the same form as that used by Bernstein et al.

$$\sigma(m_R) = (1+c)\sigma_{23}\left[10^{-\alpha_1(m_R-23)} + c10^{-\alpha_2(m_R-23)}\right]^{-1}, \quad (4)$$

with

$$c = 10^{(\alpha_2-\alpha_1)(R_{\rm eq}-23)}. \quad (5)$$

The best-fitting parameters were found to be $\sigma_{23} = 1.00$ mag^{-1} deg^{-2}, $R_{\rm eq} = 24.21$, $\alpha_1 = 1.08$ and $\alpha_2 = 0.030$, which has the interesting characteristic that the 'roll-over' magnitude $R_{\rm eq}$ moves close to the faint end of our sample with an essentially 'flat'

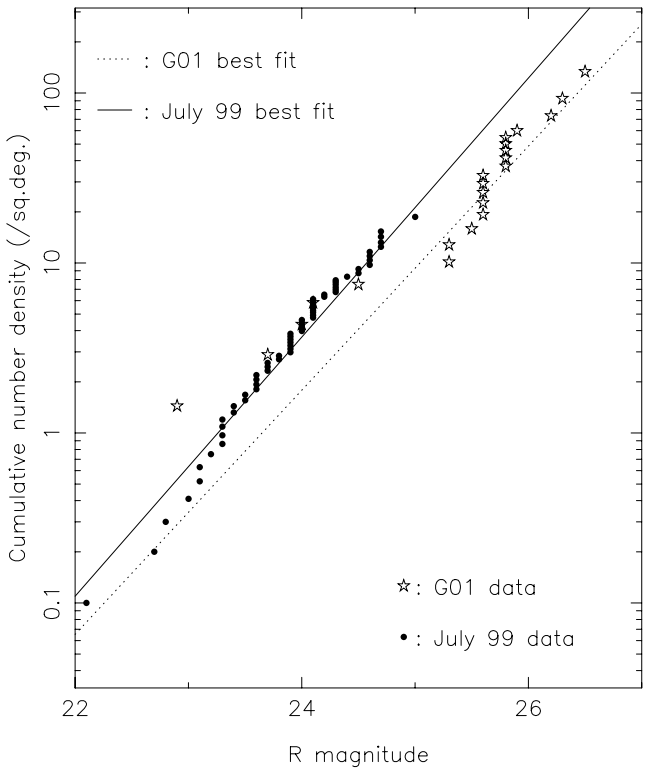

Figure 8. Debiased cumulative surface density for the present survey and for the deep survey of Gladman et al. (2001). The solid dots show the data of the present work, debiased, and the solid line represents the best-fitting single power law for these data. The open stars show the data from Gladman et al. (2001), debiased, and the dotted line represents the best-fitting single power law for these data.

function fainter than 24.2 mag (although the roll-over is not abrupt at $R_{\rm eq}$ so that the cumulative luminosity function still rises mildly). For comparison, Bernstein et al. (2004) found $\sigma_{23} = 1.08$ mag^{-1} deg^{-2}, $R_{\rm eq} = 23.6$, $\alpha_1 = 0.88$ and $\alpha_2 = 0.32$. In our opinion, the simplest conclusion from our results is that the detections do in fact follow a single power law over the observed magnitude range ($22 < m_R < 25$). As another way of approaching this question, we have computed a Bayes factor of 1.9 of the double power-law fit compared to the single power-law fit. Such a low Bayes factor (less than 3) indicates negligible support for going to the more complex model. Although clearly something must happen to the steep slope of the luminosity function in order to explain the meagre number of detections in the *HST* Advanced Camera for Surveys (ACS) experiment, our conclusion is that the data do not provide strong support for a roll-over brighter than 24 mag and that the roll-over must be deeper. To be clear, our data set provides no constraint on a model in which the luminosity function's slope becomes flatter at magnitudes fainter than $m_R = 25$.

The most similar data set to ours is the TJL01 survey, which is more difficult to interpret due to the large range of ecliptic latitudes and longitudes. Their estimate of $6.4^{+2.1}_{-1.2}$ TNOs per deg^2 brighter than $m_R = 25$ is about 7σ lower than the 20 per deg^2 predicted by our best-fitting single power-law luminosity function. In contrast to our debiased measurements, we note that the debiased differential surface-density measurements of TJL01 stop increasing at magnitudes fainter than 24 mag. As discussed in Petit et al. (2004), this would also occur in a survey where the detection efficiency is overestimated at the faintest magnitude of the survey, as might occur if the artificially implanted objects are not shown to the human operators in the same fashion as the real object candidates; this results in a spurious 'flattening' of the luminosity function's slope at the survey's limit. In contrast, we have searched our data set by implanting artificial objects before searching the data set, and thus looking at all the artificially implanted objects. We believe that this has produced the best-characterized wide-field data set available, and that the roll-over was fit by Bernstein et al. (2004) to start at 23 mag because of the presence of the roll-over in the TJL01 debiased detections, which dominates the detections in the magnitude range 23–25. Note also that the slope of the differential luminosity function of TJL01 for objects brighter than 24 mag is roughly $q = 4.6$ (see Fig. 9 in TJL01), corresponding to $\alpha = 0.72$, comparable to Gladman et al. (1998, 2001) and this work. In addition, our best-fitting single power-law luminosity function predicts a cumulative surface density of 3.4 TNOs per deg^2, while TJL01 give 3.4 ± 0.5 TNOs per deg^2 in their table 7. So both estimates do agree perfectly well down to $m_R = 24$. The recent Elliot et al. (2005) paper on the Deep Ecliptic Survey (DES) has acknowledged photometric calibration issues with possible systematic errors that render their estimate of $R_{\rm o} = 22.70 \pm 0.13$ very uncertain, with a possible shift to fainter magnitudes at the level of 0.3 or more. In addition, their detection efficiency is uncalibrated, making their slope estimate of $\alpha = 0.86 +/-0.10$ also subject to systematic errors but perhaps to a lesser extent. Taken at face value, their result is in much greater disagreement with our results than that of TJL01 due to the shape of the confidence regions in Fig. 6, and we feel confident that if the DES is calibrated, the $R_{\rm o}$ value will move to fainter magnitudes (in fact, if $R_{\rm o} = 23.4$ for their work, then the result falls in our 1σ contour).

The logical next step would be to combine this current data set with other surveys in the literature. However, we are hesitant to do this due to our concern about the complications inherent in the problem, complications that are now accessible to quantitative examination. The now-established strong dependence of the TNO sky density on latitude (Brown 2001; Trujillo & Brown 2001) makes incorporation of literature surveys problematic because they may have a large variety of latitudes. An additional wrinkle comes from the fact that the mid-plane of the Kuiper Belt is not the ecliptic, and may not be the outer Solar system's invariable plane (Brown & Pan 2004). Our previous deep survey (Gladman et al. 2001), containing 17 TNOs, was acquired at roughly 2° latitude above the invariable plane; even this can lower the sky density by roughly 30 per cent (Brown 2001). In fact, the Gladman et al. (2001) pencil-beam, in the region of magnitude overlap, is roughly this factor lower than the faint end of the new data set presented here; see Fig. 8, which compares the debiased cumulative surface densities for the present survey (solid line) and the deep survey of Gladman et al. (2001). Both surveys, taken independently, are well fitted by a single power law with index 0.76 (this work) and 0.72 (Gladman et al. 2001), with no sign of flattening at fainter magnitudes. Clearly, both curves could be seen as representing the same luminosity function or size distribution, but with a different 'zero-point' for the sky density, because the surveys were sampling different parts of the Kuiper Belt. Thus, we have chosen not to fit the new data set by adding either our older surveys or those of the literature. We believe that more homogeneous data sets with many detections in the 25–26 mag range will be required. While clearly the Bernstein et al. (2004) results demand a flattening of the luminosity at some point, our data support the conclusion that the magnitude at which the roll-over occurs is fainter than they conclude in their study. However, Bernstein et al. (2004) do not provide a credible region estimate for the roll-over

magnitude, so we cannot determine if a 25-mag roll-over is in conflict with their analysis.

5 SUMMARY

In this paper, we have presented the discovery of 65 TNOs discovered in a single homogeneous survey performed over four nights in 1999 July at the CFHT. Only 45 per cent of these were followed over several oppositions, and therefore we were interested in quantities fairly well determined already at discovery time.

The first quantity we can readily estimate at discovery time is the magnitude. A single power-law luminosity function fits perfectly our data, with a best-fitting slope of $\alpha = 0.76$ with one object per deg^2 estimated at magnitude $R_o = 23.3$. Our data can also be fitted by the double power-law luminosity function from Bernstein et al. (2004), with $\sigma_{23} = 1.00$ mag^{-1} deg^{-2}, $R_{eq} = 24.21$, $\alpha_1 = 1.08$ and $\alpha_2 = 0.030$. However, our data alone indicate negligible support for going to the more complex model. We have also shown that one cannot easily combine results from different surveys, as they may have sampled different regions of the Kuiper Belt.

In addition to the luminosity function, several authors have tried to gain some insight on other distributions, supposedly fairly well defined already at discovery time. This includes the inclination and heliocentric distance distributions. Comparing the inclination distribution at discovery to that of a subset of objects followed to multiple opposition shows that the samples are not drawn from the same sample, impairing such a derivation with only short orbital arcs. Note however that our arcs were very short (less than 2 h), while most short-arc objects in the MPC data base have an arc length of 24 h or more. In this case, the inclination determination becomes valid. The heliocentric distance distribution is more robust even at discovery, and our data support the claim for a sudden drop in surface density of the Kuiper Belt beyond the 2 : 1 resonance.

ACKNOWLEDGMENTS

This work was supported by a Henri Chrétien international research grant (AAS), by National Aeronautics and Space Administration (NASA) Origins grants NAG5-8198, NAG5-9678 and NAG5-10365, by an ACI Jeune award from the French Research Ministry, and by an Observatoire de la Côte d'Azur BQR grant.

BJG, JJK, J-MP and MJH were visiting astronomers at the CFHT, operated by the National Research Council of Canada, Centre National de la Recherche Scientifique de France, and the University of Hawaii.

Some of the analysis presented here uses the Python INFERENCE package developed by TJL with support from NASA grant NAG5-12082.

REFERENCES

Allen R. L., Bernstein G. M., Malhotra R., 2002, AJ, 124, 2949
Bernstein G., Khushalani B., 2000, AJ, 120, 3323
Bernstein G. M., Trilling D. E., Allen R. L., Brown M. E., Holman M., Malhotra R., 2004, AJ, 128, 1364
Brown M. E., 2001, AJ, 121, 2804
Brown M. E., Pan M., 2004, AJ, 127, 2418
Chiang E. I., Brown M. E., 1999, AJ, 118, 1411
Cuillandre J.-C., Luppino G., Starr B., Isani S., 1999, in Amico P., Beletic J. W., eds, Optical Detectors for Astronomy, Proc. 4th ESO CCD Workshop. Kluwer, Dordrecht
Davis D. R., Farinella P., 1996, Icarus, 125, 50
Dones L., 1997, in Pendleton Y. J., Tielens A. G. G. M., eds, ASP Conf. Ser. Vol. 122, From Stardust to Planetesimals. Astron. Soc. Pac., San Francisco, p. 347
Doressoundiram A., Peixinho N., Doucet C., Mousia O., Barucci M. A., Petit J.-M., Veillet C., 2005, Icarus, 174, 90
Elliot J. L. et al., 2005, AJ, 129, 1117
Gladman B., Kavelaars J. J., Nicholson P., Loredo T., Burns J. A., 1998, AJ, 116, 2042
Gladman B., Kavelaars J. J., Holman H., Petit J.-M., Scholl H., Nicholson P., Burns J. A., 2000, Icarus, 147, 320
Gladman B., Kavelaars J. J., Petit J.-M., Morbidelli A., Holman M. J., Loredo T., 2001, AJ, 122, 1051
Jewitt D. C., Luu J. X., Trujillo C., 1998, AJ, 115, 2125
Kenyon S. J., Bromley B. C., 2004, AJ, 128, 1916
Kraft R., Burrows D., Nouaek J. A., 1991, ApJ, 374, 344
Landolt A., 1992, AJ, 104, 340
Larsen J. A. et al., 2001, AJ, 121, 562
Levison H. F., Morbidelli A., 2003, Nat, 426, 419
Petit J.-M., Holman M., Scholl H., Kavelaars J. J., Gladman B., 2004, MNRAS, 347, 471
Press W. H., Teukolsky S. A., Vetterling W. F., Flannery B. P., 1992, in Press W. H., ed., Numerical Recipes in Fortran: the Art of Scientific Computing, 2nd edn. Cambridge Univ. Press, Cambridge
Trujillo C. A., Brown M. E., 2001, ApJ, 554, L95
Trujillo C. A., Brown M. E., 2003, Earth, Moon and Planets, 92, 99
Trujillo C. A., Jewitt D. C., Luu J. X., 2001a, AJ, 122, 457 (TJL01)
Trujillo C. A., Luu J. X., Bosh A. S., Elliot J. L., 2001b, AJ, 122, 2740
Weidenschilling S., 2003, in Proc. 34th Annual Lunar and Planetary Science Conf. Vol. 34. Lunar and Planetary Institute, Houston, TX, p. 1707

This paper has been typeset from a TEX/LATEX file prepared by the author.